Development of a low-cost quadrotor UAV based on ADRC for agricultural remote sensing

Songchao Zhang[1,2], Xinyu Xue[1*], Chen Chen[1], Zhu Sun[1], Tao Sun[1]

(1. *Nanjing Research Institute for Agricultural Mechanization, Ministry of Agriculture and Rural Affairs, Nanjing 210014, China*; 2. *Key Laboratory of Modern Agricultural Equipment and Technology, Ministry of Education, Jiangsu University, Zhenjiang 212013, China*)

Abstract: Unmanned aerial vehicle (UAV) has the advantages of good repeatability and high remote sensing (RS) information acquisition efficiency, as an important supplement bridging the gap of high-altitude and ground RS platforms. A quadrotor UAV was developed for the agricultural RS application in this study. The control system consists of a main processor and a coprocessor, integrating a three-axis gyroscope, a three-axis accelerometer, an air pressure sensor and a global positioning system (GPS) module. Engineering trial method (ETM) was used to tune the parameters based on the active disturbance rejection control (ADRC) method. Also a ground control station (GCS) adapted to the quadrotor was developed realizing autonomously take-off and landing, flight route planning, data recording. To investigate the performances of the UAV, several flight tests were carried out. The test results showed that the pitch angle control accuracy error was less than 4°, the flight height control accuracy error was less than 0.86 m, the flight path control accuracy error was less than 1.5 m overall. Aerial multispectral images were acquired and processed. The reflected digital number (DN) values obtained from a height of 10-100 m with 10 m interval could be referenced to classify objects. The normalized-difference-vegetation index (NDVI) values obtained from the aerial multispectral images acquired at 15 m were compared with those obtained by the GreenSeeker (GS) and PSR-1100F. The maximum error was 20.37% while the minimum error was 1.99%, which demonstrated the developed quadrotor UAV's satisfactions for low altitude remote sensing practice. This study provided a low-cost platform for agricultural remote sensing.

Keywords: UAV, quadrotor, ADRC, agricultural remote sensing, NDVI, aerial spraying application

DOI: 10.25165/j.ijabe.20191204.4641

Citation: Zhang S C, Xue X Y, Chen C, Sun Z, Sun T. Development of a low-cost quadrotor UAV based on ADRC for agricultural remote sensing. Int J Agric & Biol Eng, 2019; 12(4): 82–87.

1 Introduction

Unmanned Aerial Vehicle (UAV) has been widely used in precision agriculture with its superior performances, including aerial spraying application[1-4], auxiliary pollination[5], remote sensing information acquisition[6-10], disaster forewarning[11] etc. As a remote sensing platform, the UAV has the features of low cost, strong mobility, well repeatability and continuous dynamic monitoring, by which the information obtained could supplement the temporal and spatial resolution of high-altitude and ground remote sensing[12-16].

Consequently, recent years UAV-based agricultural remote-sensing systems have been developed by some researchers. Bagheri[17] developed a high-resolution aerial remote-sensing system for precision agriculture. This system consisted of on-board and ground station subsystems. A telemetry system was used to communicate between the on-board and ground-station subsystems. The multispectral imageries were obtained based on the system from a height of 10-250 m and were processed and evaluated. The spatial resolution of the multispectral imagery obtained was 3.6-95 mm/pixel, respectively, the supervised classification map overall accuracy was 94% and kappa coefficient was 0.9. Aldana-Jague et al.[18] used UAV multispectral imagery for estimating the soil organic carbon (SOC) content. The results showed that the methodology had a clear potential for use in precision agriculture or monitoring important soil properties following changes in management. Vega et al.[19] used multi-temporal images to monitor a sunflower crop during the growing season by the UAV. The results showed that the linear regressions between NDVI and grain yield, aerial biomass and nitrogen content in the biomass were significant at the 99% confidence level, except during very early growth stages. Garcia-Ruiz et al.[20] used a UAV for plant detection via a multi-band imaging sensor and the results were compared with those of aircraft-based sensors. The accuracy of the classified images acquired by the UAV and aircraft was 61%-74% on seven vegetation indexes and 67%-85% during six spectral bands (from 530 to 900 nm), respectively. Classified maps were produced based on the NDVI by Primicerio et al.[21] via a six-rotor UAV for site-specific vineyard management. The results showed clearly crop heterogeneity conditions in good agreement with ground-based observations.

Multi-rotor UAV generally adopts a symmetrical structure layout for the better stability, and the structure has high degree of modularity, simply and easily to fold and disassemble. It is usually driven by batteries, adjusting the flying attitudes by

Received data: 2018-09-07 **Accepted data:** 2019-03-08

Biographies: Songchao Zhang, MS, research interests: precise pesticide spraying, Email: 51832898@qq.com; **Chen Chen**, MS, research interests: precise pesticide spraying, Email: 3043095@163.com; **Zhu Sun**, BS, research interests: detection and control, Email: 43148588@qq.com; **Tao Sun,** MS, research interests: precise pesticide spraying, Email: 2260559763@163.com.

***Corresponding author: Xinyu Xue,** PhD, Professor, research interest: crop protection and machinery engineering, Nanjing Research Institute for Agricultural Mechanization, Ministry of Agriculture, Nanjing 210014, China. Tel: +86-25-84346243, Email: xuexynj@qq.com.

changing the corresponding motor speed. However, multi-rotor UAV is a typical underactuated system with multivariable, nonlinear, strong coupling and interference-sensitive properties[22,23]. In order to achieve effective control of multi-rotor UAV, some researches have been conducted. Liao et al.[24] adopted the dual closed-loop PID (proportion, integration, differentiation) control strategy to realize the stable control and enhance its anti-interference ability. Shan[25] proposed that expert system control algorithm (ESCA) should be used in the design of the quadrotor. Sun[26] designed intelligent proportional and integral controllers, realizing the rapid recovery of attitude angle to the equilibrium. Liu et al.[27] applied fuzzy PID control algorithm to achieve stable flight of plant protection quadrotor UAV.

ADRC is a control method developed on the basis of PID by setting a tracking differentiator (TD) to arrange the transition process and extract the differential signals, an extended state observer (ESO) to estimate the control object's state and the uncertain disturbance, finally a nonlinear state error feedback (NLSEF) is formed through the nonlinear combination of the results from the TD and ESO, also including the compensation for external disturbances if needed[28-30].

A quadrotor UAV was developed for the agricultural RS based on ADRC in this article. Test results including the flight stabilities, aerial image acquirement and vegetation index analysis proved the UAV could meet the agricultural RS practice requirements.

2 Materials and methods

2.1 The quadrotor UAV

2.1.1 Analysis of the motion

The mechanism and force analysis of the *X*-type quadrotor UAV is shown in Figure 1, where the *X*-axis direction is forward.

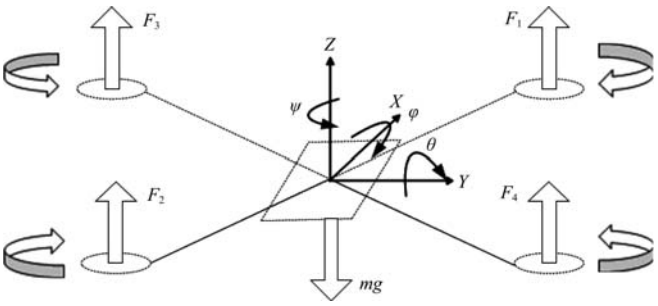

Figure 1 The mechanism and force analysis of the quadrotor UAV

According to the moment of momentum theorem, the quadrotor UAV model could be defined as the follow equations[30].

$$\begin{cases} \ddot{x} = U_1(\sin\psi\sin\varphi + \cos\psi\sin\theta\cos\varphi)m^{-1} \\ \ddot{y} = U_1(\sin\psi\sin\theta\cos\varphi - \cos\psi\sin\varphi)m^{-1} \\ \ddot{z} = U_1\cos\varphi\cos\theta m^{-1} - g \\ \ddot{\varphi} = U_2 l I_x^{-1} \\ \ddot{\theta} = U_3 l I_y^{-1} \\ \ddot{\psi} = U_4 \lambda I_z^{-1} \end{cases} \quad (1)$$

where, $\ddot{x}$, $\ddot{y}$, $\ddot{z}$ are the vectors of the UAV position; $\ddot{\varphi}$, $\ddot{\theta}$, $\ddot{\psi}$ are the roll angle, pitch angle and yaw angle; m is the quality; l is the length from the end of a rotor to the center of the gravity(the arm length); λ is the ratio between the torsion moment generated by the lift force to the lift force; I_x, I_y, I_z refer to the moments of inertia of the UAV body around *X*, *Y*, *Z* axes, respectively; U_1, U_2, U_3, U_4 are the four independent inputs of the nonlinear coupling UAV model, calculated by the equation (2). The UAV arises (or descends) when U_1 is greater (or less) than mg, the UAV rolls when U_2 is greater or less than zero, the UAV pitches when U_3 is greater or less than zero, while the UAV yaws when U_4 is greater or less than zero with an unbalanced torque.

$$\begin{cases} U_1 = F_1 + F_2 + F_3 + F_4 \\ U_2 = F_1 + F_4 - F_2 - F_3 \\ U_3 = F_1 + F_3 - F_2 - F_4 \\ U_4 = F_1 + F_2 - F_3 - F_4 \end{cases} \quad (2)$$

2.1.2 Platform framework and power source

The LF4X300 type carbon fiber frame was adopted with 700 mm wheelbase and double pipe fixed feet. The T-Motor 3080 type carbon fiber propellers were selected for its high strength and light weight. The power source was from two 6S1P high-voltage version lithium batteries in series with capacity of 16000 mA·h, sustained discharge rate of 15C, and peak discharge rate of 30C. The electronic speed controller (ESC) of HV80A realized adjusting the input direct current for driving brushless motor and adjusting the motor according from the control signals. The four brushless motors (Q9XL-120KV) combined with the T-Motor 3080 propellers could generate about 220 N pulling force, satisfying the requirements of 20 kg load.

2.1.3 Control unit and core sensors

As the main control unit, the microprogrammed control unit (MCU) STM32F427 with CortexTM-M4 kernel, 180 MHz frequency, 2MB Flash ROM (read only memory) and 256KB SRAM (static random access memory), communicates with the triaxial gyroscope L3GD20H, the triaxial accelerometer/ magnetometer LSM303D, and the barometer MS5611 through two inter-integrated circuit (I2C). The MCU STM32F103 as a coprocessor performs code and function redundancy and is responsible for failure protection and firmware upgrade.

The L3GD20H module integrates micro-electro-mechanical system (MEMS) to measure the 3-axis angular velocity for acquitting the dynamic attitude of the UAV. The core chip size is 3 mm×3 mm×1 mm, accuracy is ±500 DPS (degree per second) with 16-bit digital output. The LSM303D chip integrates accelerometer and magnetometer functions with 12-bit digital output. The maximum range of linear acceleration is ±16 g with high pass filter to eliminate temperature effect on zero, the maximum range of magnetic field strength is ±12 gauss with set/reset circuit to restore anisotropic magneto resistance (AMR) before each measurement of the magnetic domain. The MS5611 package integrates a 24-bit digital air pressure sensor with a size of 5 mm×3 mm ×1 mm, a resolution up to 10 cm. Ublox-NEO-M8N GPS module is used for positioning and navigation.

2.1.4 Cost estimation

In this research, hardware system mainly includes the LF4X300 type carbon fiber frame (about 1300 RMB), four brushless motors of Q9XL-120KV (about 4×450 RMB), four T-Motor 3080 type carbon fiber propellers (about 4×250 RMB), two 6S1P high-voltage version lithium batteries (about 2×1200 RMB), four electronic speed controller (ESC) of HV80A (4×480 RMB), a PX4 Flight-Control board integrated with the MCU STM32F427, STM32F103, the triaxial gyroscope L3GD20H, the triaxial accelerometer/ magnetometer LSM303D, the barometer MS5611 (about 1800RMB), and the Ublox-NEO-M8N GPS module (about 60RMB), which are easily bought online or on the market. The total cost is about 10300 RMB (1535 USD dollars)

plus the lines, cushions etc. Considering the UAV can realize the functions of planning route, autonomous flight, fixed-point photographing, etc. the cost is relatively low.

2.2 ADRC Controller Design and Parameter Tuning

The low order ADRC controllers are more widely used in practical applications, the Figure 2 shows the second-order ADRC controller structure.

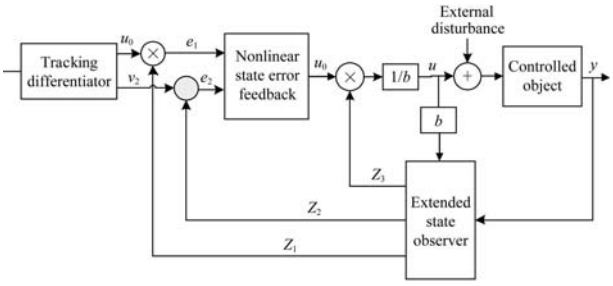

Figure 2 Structure of ADRC controller

2.2.1 ADRC algorithm model

ADRC algorithm model includes TD, ESO and NLSEF.

TD smooths and differentiates the signal according to the reference input and the output of the control object, balancing the contradiction of overshoot and fast response. The common mathematical expression equation is as below.

$$\begin{cases} v_1(t+h) = v_1(t) + hv_2(t) \\ v_2(t+h) = v_2(t) + hfhan(v_1(t) - v\ (t), v_2(t), r, h) \end{cases} \tag{3}$$

where, $v(t)$ is the input signal; h is the integral step; r is the tracking factor; *fhan* is the nonlinear function defined as below.

$$fhan = \begin{cases} -r\dfrac{a}{d}, & |a| \le d \\ -r\,\mathrm{sgn}(a), & |a| > d \end{cases} \tag{4}$$

$$a_0 = \sqrt{d^2 + 8r|y|} \tag{5}$$

$$a = \begin{cases} v_2 + \dfrac{\mathrm{sgn}(y)(a_0 - d)}{2}, & |y| > d_0 \\ v_2 + \dfrac{y}{h_0}, & |y| \le d_0 \end{cases} \tag{6}$$

$$y = v_1 - v + hv_2 \tag{7}$$

$$d = rh,\ d_0 = hd \tag{8}$$

ESO feeds back and compensates for the system to achieve more stable control taken the unknown external interferences into account.

$$\begin{cases} e = z_1 - y \\ \dot{z}_1 = z_2 - \beta_{01}e \\ \dot{z}_2 = z_3 - \beta_{02}fal(e, \alpha_1, \delta_1)b * u \\ \dot{z}_3 = -\beta_{03}fal(e, \alpha_2, \delta_1) \end{cases} \tag{9}$$

where, z_1, z_2 are the estimated state variables of the signal y; z_3 is the estimated state variable of the total interference; e is the error; α_1, α_2, δ_1, β_{01}, β_{02}, β_{03} are the parameters to be tuned, and the nonlinear function *fal* is defined as follow.

$$fal(e, \alpha, \delta) = \begin{cases} \dfrac{e}{\delta^{1-\alpha}}, & |e| \le \delta \\ |e|^{\alpha}\,\mathrm{sgn}(e), & |e| > \delta \end{cases} \tag{10}$$

NLSEF is a non-linear combination of the differential inputs (v_1, v_2) from the TD and the errors (e_1, e_2) from the ESO, then outputs with the total interference.

$$u_0 = \beta_1 fal(e_1, \alpha_3, \delta_0) + \beta_2 fal(e_2, \alpha_4, \delta_0) \tag{11}$$

where, α_3, α_4, δ_0, β_1, β_2 are the parameters to be tuned.

2.2.2 Parameters tuned

The parameters needed to be tuned in ADRC controller include the integral step h, tracking factor r of the TD, α_1, α_2, δ_1, β_{01}, β_{02}, β_{03} of the ESO, α_3, α_4, δ_0, β_1, β_2 of NLSEF. The value of r directly affects the response time, larger value for shorter response time, meanwhile greater overshoot. The values of β_{01}, β_{02}, β_{03} directly affect the dynamic characteristics of closed loop system. The value of β_1 affects the adjust speed, increase the value of β_2 could inhibit overshoot and reduce oscillation.

ETM was used to tune the parameters on the references of other conclusions[28-31], and some simulations were carried out to verify the tuned parameters. Due to the limitation of space, the results of the tuned parameters are directly given as shown in Table 1.

Table 1 The tuned parameters of ADRC

Parameters	h_0	h	r	α_1	α_2	δ_1	β_{01}	β_{02}	β_{03}	α_3	α_4	δ_0	β_1	β_2
Values	0.001	0.001	1600	0.5	0.25	0.01	1000	1000	1000	0.5	0.25	0.01	200	300

3 Test analysis and discussion

Figure 3 shows the final developed quadrotor UAV for RS. A GCS was developed based on the open source software Mission Planner and the communication protocol MAVLink. The control accuracy and aerial multispectral image acquisition tests were conducted.

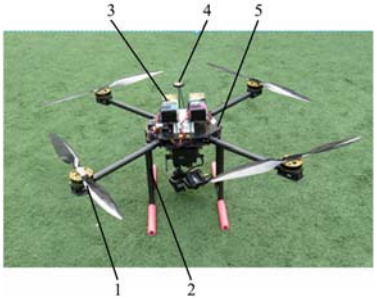

1. Motor and rotor 2. Fuselage 3. Batteries 4. GPS antenna 5. Control circuit board

Figure 3 The quadrotor UAV for RS

3.1 Control accuracy tests

The tests were carried out outdoor as Figure 4 with less than 3 m/s average wind speed. The UAV was set as hovering flight at 5 m lasting for 4 min, the GCS recorded the pitch angles through the telemetry with 10 Hz sampling frequency. For the altitude and trajectory accuracy tests, four ground marking points were set as a 20 m×20 m square, each GPS coordinate of the point was recorded and connection of the four point-coordinates formed the UAV flight path. The UAV was set flying at 20 m height, the height and trajectory were recorded via the GCS. The results showed that the pitch angle control error between ±4°, the flight altitude control error between ±0.86 m, the flight path control error less than 1.5 m totally. Figure 5 shows the pitch angle test results in which the expected value was set as 0°.

3.2 Aerial multispectral image acquisition and analysis

A multi-spectral camera (ADC Lite, Tetracam Inc, Gainesville, FL, USA) was mounted to acquire aerial images for verifying the practicability of the quadrotor UAV at Baima base Nanjing Lishui of Jiangsu province, China (119.19117°E, 31.60644°N).

The crop canopy multi-spectral images of 10-100 m height were acquired with a 10 m interval. Non-standard whiteboards were used as control points on the ground to facilitate the extraction of image information. The NDVI values were extracted and compared with the data measured by GS (Trimble Ag, USA) and calculated by PSR-1100F (Spectral Evolution Co. Ltd , USA) as the basis. Figure 6 shows the multispectral images (false colored) collected at heights of 70 m, 80 m, 90 m and 100 m. The non-standard whiteboard as object 1(O1), cement pavement as object 2(O2), soil as object 3(O3) and crop as object 4(O4) could be clearly distinguished.

1. Ground marking point 2. UAV

Figure 4 Fly test of quadrotor UAV

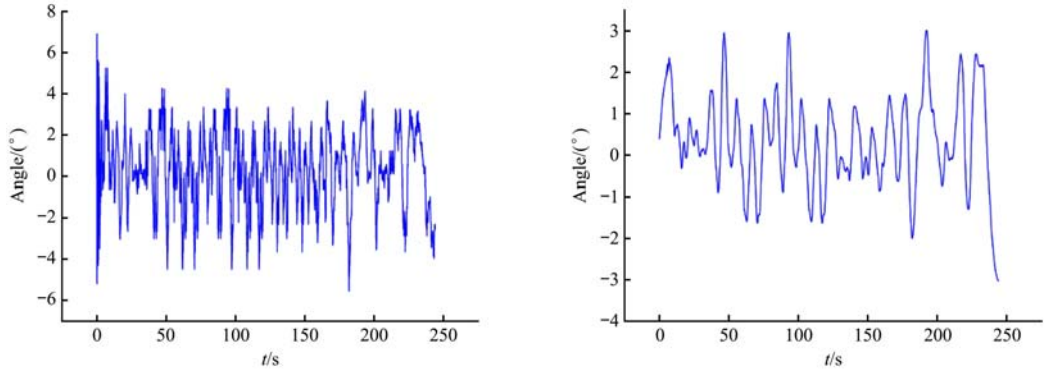

a. Raw pitch angles b. Smoothed pitch angles

Figure 5 Pitch angle test results

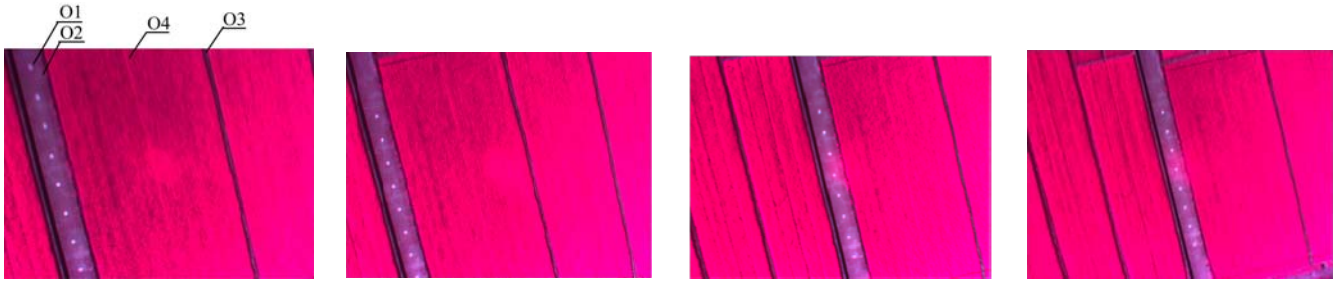

a. Multispectral image of 70 m b. Multispectral image of 80 m c. Multispectral image of 90 m d. Multispectral image of 100 m

Figure 6 Aerial multispectral images acquired at different height

3.2.1 Multispectral imagery classification

The three band (green, red, near-infrared) reflect DN values of O1, O2, O3, O4, O5 were statistically analyzed in PixelWrench2 selecting the appropriate exposure areas (8-bit, 256 levels), showed in Table 2. The O5 is the teflon plate calibrated with the camera as the standard reference whiteboard.

Table 2 Statistics of reflect DN values

Row	Object	Green band	Red band	Near infrared band	Standard deviation (%)
1	O1	195-206	189-214	187-215	3.44, 7.74, 7.72
2	O2	30-76	42-81	51-86	16.21, 12.02, 11.31
3	O3	48-85	52-91	46-87	12.34, 13.11, 12.93
4	O4	140-192	33-58	169-218	17.81, 10.85, 13.38
5	O5	247-255	243-255	229-255	2.63, 3.05, 7.06

The O5 has the highest reflect levels, the minimum DN value is 229 (near-infrared band), the maximum value is 255, and the standard deviation of the three bands is the smallest for 2.63%, 3.05% and 7.06%, which indicates that O5 could be used as standard whiteboard. Its reflection value (DN value) was used to calibrate the other objects. The calibration calculation equations are as follow.

$$DN_{cali-Oi} = \frac{DN_{oi}}{DN_{o5}} \times 255 \tag{10}$$

where, $DN_{cali-Oi}$ is the calibrated DN value each band of Oi, Oi are O1 to O4; DN_{o5} is the corresponding DN band value of O5.

The O1 is a medium of calculating the vegetation index, the DN values ranged from 187 to 215 with standard deviations of 3.44%, 7.74%, and 7.72%, indicating that the non-standard whiteboard had good chroma uniformity.

Classified from the reflection intensity, the DN values of O2, O3 are almost less than 90 (based on 256 levels) at the three bands because of the low surface reflectance, while the DN values of O4 are greater than 140 at green band and near-infrared band because of the strong absorption at red band.

3.2.2 Three channel image and NDVI index verification

In order to reduce the influence of atmospheric path radiation, another series of aerial multispectral images were acquired at 15 m. Figure 7 shows the false color, green channel, red and near-infrared channel images. Due to the different absorption of green, red, and near-infrared light by the crop, the brightness of the three-channel image matches expectations.

The average NDVI values of ten sample points were calculated and compared with the values obtained by the ground methods. The Figure 8 is the one of the NDVI value classification image, the value range is during –0.216 to 0.788. The Figure 9 shows the average NDVI values from the aerial images and the GS. The values from the GS are generally less than those from the aerial

images, the ratio is between 0.83-0.98 except the sample point 1(S1). Assume the GS NDVI value as the true value, the maximum relative error of the aerial image NDVI value is 20.37% (S6), and the minimum relative error is 1.99% (S5). The reason for the analysis results may because of using O5 to standardize O1 in calibrating the reflectance with the ignoring of atmospheric path radiation, the near-infrared band reflectance (R_{NIR}) increases while the red band reflectance (R_{red}) decreases, and (R_{NIR}-R_{red}) increases larger than (R_{NIR}+R_{red}) does.

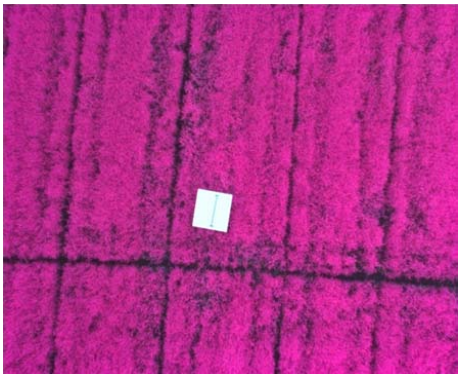

a. False color image

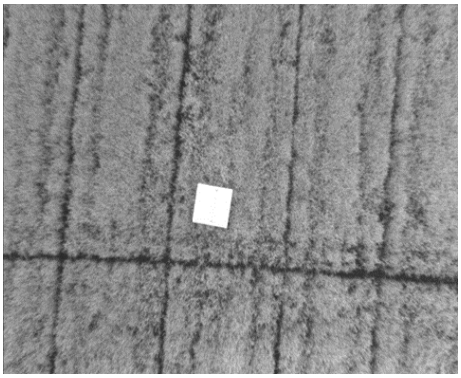

b. Green channel image

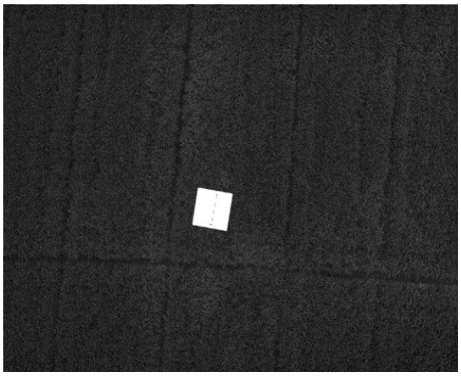

c. Red channel image

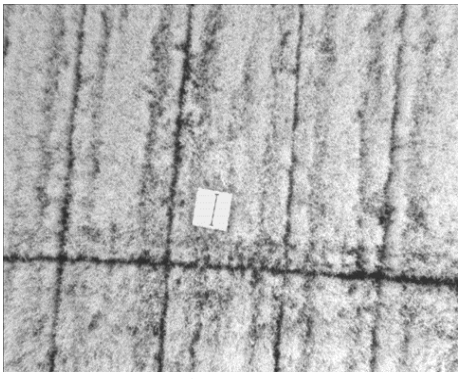

d. Near-infrared channel image

Figure 7 Processed aerial images of different channels

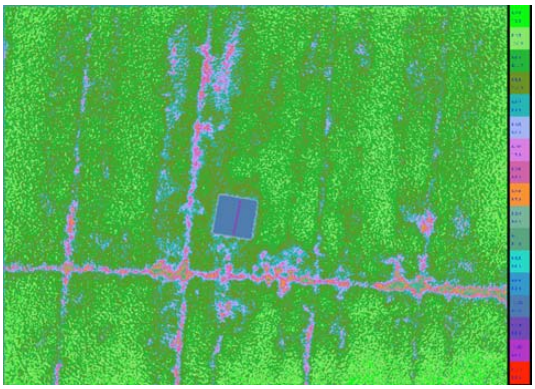

Figure 8 NDVI value classification image

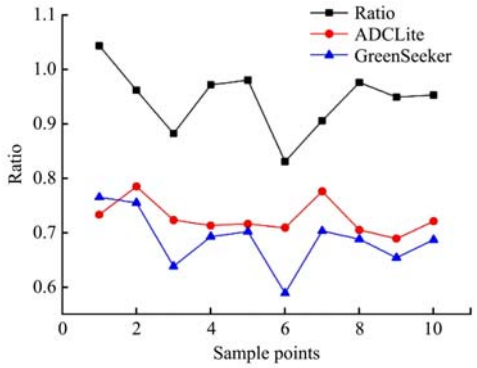

Figure 9 Comparisons of NDVI values

4 Conclusions

Due to the advantages of low cost and flexibility, the application of UAVs in agriculture is increasing nowadays. The crop remote sensing information acquisition is an important application direction, so it is necessary to develop a UAV that meets requirements according to different needs. Thus, a quadrotor UAV was developed based on the ADRC controller and evaluated for low altitude remote sensing practice. Based on the results, the main conclusions are discussed as follow.

The hovering flight and the planned flight test results demonstrated that the UAV was reliable and showed a good ability to perform the desired tasks, which the pitch angle control accuracy error was less than 4°, and the flight height control accuracy error was less than 0.86 m, the flight path control accuracy error was less than 1.5 m overall. The aerial multispectral images acquisition of different heights could be used to distinguish objects by the visualized false color images and DN values easily based on the UAV system. The NDVI values obtained from the aerial and ground were compared, the maximum relative error was 20.37% while the minimum relative error was 1.99%, which proved the UAV's applicability in agricultural remote sensing further.

Acknowledgements

This research was financially supported by the National Natural Science Foundation of China (No.31701327), the National Key Research and Development Program of China (Grant NO. 2017YFD0701000), Collaborative Innovation Plan of Scientific and Technological Innovation Project (Grant No. CAAS-XTCX2016006).

[References]

[1] Yang F B, Xue X Y, Cai C, Zhou Q Q. Effect of down wash airflow in hover on droplet motion law for multi-rotor unmanned plant protection

machine. Transactions of the CSAE, 2018; 34(2): 64–73. (in Chinese)
[2] Xue X Y, Lan Y B, Sun Z, Chang C, Hoffmann W C. Develop an unmanned aerial vehicle based automatic aerial spraying system. Computers & Electronics in Agriculture, 2016; 128: 58–66.
[3] Zhang S C, Xue X Y, Qin W C, Sun Z, Ding S M, Zhou L X. Simulation and experimental verification of aerial spraying drift on N-3 unmanned spraying helicopter. Transactions of the CSAE, 2015; 31(3): 87–93. (in Chinese)
[4] Xue X Y, Tu K, Qin W C, Lan Y B, Zhang H H. Drift and deposition of ultra-low altitude and low volume application in paddy field. Int J Agric & Biol Eng, 2014; 7(4): 23–28.
[5] Li J, Zhou Z, Hu L, Zhang Y, Yan M, Liu A, et al. Optimization of operation parameters for supplementary pollination in hybrid rice breeding using round multi-axis multi-rotor electric unmanned helicopter. Transactions of the CSAE, 2014; 30(11): 1–9. (in Chinese)
[6] Shi Z, Liang Z Z, Yang Y Y, Guo Y. Status and prospect of agricultural remote sensing. Transactions of the CSAM, 2015; 46(2): 247–260. (in Chinese)
[7] Lamb D W. The use of qualitative airborne multispectral imaging for managing agricultural crops--a case study in south-eastern Australia. Australian Journal of Experimental Agriculture, 2000; 40(40): 725–738.
[8] Li M, Huang Y Q, Li X M, Peng D X, Xie J X. Extraction of rice planting information based on remote sensing image from UAV. Transactions of the CSAE, 2018; 34(4): 108–114. (in Chinese)
[9] Wang X Q, Wang M M, Wang S Q, Wu Y D. Extraction of vegetation information from visible unmanned aerial vehicle images. Transactions of the CSAE, 2015; 31(5): 152–159. (in Chinese)
[10] Poblete-Echeverría C, Olmedo G F, Ingram B, Bardeen M D. Detection and segmentation of vine canopy in ultra-high spatial resolution RGB imagery obtained from unmanned aerial vehicle (UAV): A case study in a commercial vineyard. Remote Sensing, 2017; 9(268): 14.
[11] Gan P, Dong Y S, Sun L, Yang G J, Li Z H, Yang F, et al. Evaluation of maize waterlogging disaster using UAV LiDAR data. Scientia Agricultura Sinica, 2017; 50(15): 2983–2992. (in Chinese)
[12] Sims D A, Gamon J A. Relationships between leaf pigment content and spectral reflectance across a wide range of species, leaf structures and developmental stages. Remote Sensing of Environment, 2002; 81(2): 337–354.
[13] Bunting P, Lucas R. The delineation of tree crowns in Australian mixed species forests using hyperspectral Compact Airborne Spectrographic Imager (CASI) data. Remote Sensing of Environment, 2006; 101(2): 230–248.
[14] Camille L, Philippe B, Guillaume J, Bruno R, Labbé S, Baret F. Assessment of unmanned aerial vehicles imagery for quantitative monitoring of wheat crop in small plots. Sensors, 2008; 8(5): 3557–3585.
[15] Huang Y B, Thomson S J, Hoffmann W C, Lan Y B, Fritz B K. Development and prospect of unmanned aerial vehicle technologies for agricultural production management. Int J Agric & Biol Eng, 2013; 6(3): 1–10.
[16] Wang P, Luo X, Zhou Z, Zang Y, Hu L. Key technology for remote sensing information acquisition based on micro UAV. Transactions of the CSAE, 2014; 30(18): 1–12. (in Chinese)
[17] Bagheri N. Development of a high-resolution aerial remote-sensing system for precision agriculture. Taylor & Francis, Inc. 2017; 38(21): 1–13.
[18] Emilien A J, Goswin H, Andy M, Bas V W, Krist of V O. UAS-based soil carbon mapping using VIS-NIR (480-1000 nm) multi-spectral imaging: Potential and limitations. Geoderma, 2016; 275: 55–66.
[19] Francisco A V, Fernando C R, Monica P S, Francisco O R. Multi-temporal imaging using an unmanned aerial vehicle for monitoring a sunflower crop. Biosystems Engineering, 2015; 132(13): 19–27.
[20] Francisco G R, Sindhuja S, Joe M M, Won S L, Jesper R. Comparison of two aerial imaging platforms for identification of Huanglongbing-infected citrus trees. Computers & Electronics in Agriculture, 2013; 91(91): 106–115.
[21] Primicerio, J, Gennaro, S F D, Fiorillo, E, Genesio, L, Lugato, E, Matese, A, et al. A flexible unmanned aerial vehicle for precision agriculture. Precision Agriculture, 2012; 13(4): 517–523.
[22] Wang X H, Liu J K, Cai K Y. Tracking control for a velocity-sensorless VTOL aircraft with delayed outputs. Automatica, 2009; 45(12): 2876–2882.
[23] Li J, Qi X H, Han S T. Attitude decoupling control for quadrotor aircraft based on active disturbance rejection control technique. Electronics Optics & Control, 2013; 20(3): 44–48. (in Chinese)
[24] Liao Y H, Zhang T M, Lan Y B. Design and test of attitude stabilization control system of multi-rotor unmanned aerial vehicle applied in farmland information acquisition. Transactions of the CSAE, 2017; 33(3): 88–98. (in Chinese)
[25] Shan H Y. Research on flight control technology of a quad-rotor unmanned helicopter. Nanjing: Nanjing University of Aeronautics and Astronautics, 2008. (in Chinese)
[26] Sun P. PID attitude control and experimental research of the mini unmanned helicopter. Changsha: National University of Defense Technology, 2008.
[27] Liu H P, Long C J, Wan P, Wang X Y, Hu B. Fuzzy self-adjusting proportion integration differentiation for eppo quadrocopter. Transactions of the CSAE, 2015; 31(1): 71–77. (in Chinese)
[28] Han J Q. From PID technique to active disturbances rejection control technique. Control Engineering of China, 2002; 9(3): 13–18. (in Chinese)
[29] Yu X N, Zhu L L. Dynamic parameter setting and application of active disturbance rejection controller. Journal of North China Electric Power University, 2005; 32(6): 9–13. (in Chinese)
[30] Yang L B, Zhang W G, Huang D G. Robust trajectory tracking for quadrotor aircraft based on ADRC attitude decoupling control. Journal of Beijing University of Aeronautics & Astronautics, 2015; 41(6): 1026–1033.
[31] Guo Q Q. Study on design and control method for mini-quadrotor UAV control system. Changchun: Jilin University, 2013. (in Chinese)